Influence of electronic effects on the surface erosion of tungsten

S. Khakshouri[1] and D. M. Duffy[1,2]

[1]*Department of Physics and Astronomy, Materials Simulation Laboratory and London Centre for Nanotechnology,*
University College London, Gower Street, London WC1E 6BT, United Kingdom
[2]*EURATOM/UKAEA Fusion Association, Culham Science Centre, Oxfordshire OX14 3DB, United Kingdom*

Tungsten is a strong contender for a plasma-facing material in future fusion power plant designs, and the material of choice for the divertor of ITER, due to its high melting point, thermal conductivity, and resistance to sputtering erosion. Sputtering erosion is a major concern for plasma-facing materials because sputtered atoms could enter the plasma and result in cooling. Atomistic modeling, using molecular dynamics, has previously been successful in identifying fundamental mechanisms of surface damage caused by ion bombardment. The damage has been found to be particularly sensitive to the rate of energy dissipation but energy transport is not well described in classical molecular dynamics simulations of metals. We present a methodology for including a realistic description of electronic energy absorption, transport, and redistribution in molecular dynamics simulations of self sputtering. The results for three different 5 keV self-sputtering events are presented for four distinct thermal transport models. The results demonstrate the sensitivity of surface damage to the model used to describe the electronic thermal transport.

I. INTRODUCTION

Tungsten (W) has been proposed as a candidate material for plasma-facing components in fusion reactors[1,2] due to its high melting point, thermal conductivity, and resistance to sputtering erosion by hydrogen bombardment. Sputtering erosion is particularly important for plasma-facing materials because the sputtered atoms may enter the plasma and the subsequent ionization results in plasma cooling. The sputtered atoms may also be redeposited on the surface and it has been suggested that the surface erosion due to the redeposition of sputtered W atoms may be orders of magnitude higher than the erosion due to hydrogen bombardment.[3]

Simulation plays a key role in the assessment of materials for fusion applications due to the difficulty and expense of recreating reactor conditions experimentally. The bombardment of a surface by ions in the keV energy range can be studied using classical molecular dynamics (MD) simulations.[4–7] The use of this technique in studying the microscopic phenomena underlying radiation damage has a long and successful history. In particular, Ghaly *et al.*[5] have identified three surface-damage mechanisms: ballistic damage, viscous flow, and microexplosions caused by particle bombardment. Each mechanism gives distinct surface features. The mechanism that dominates for a particular sputtering event depends on the properties of the material (melting temperature, density) and the properties of the bombarding atom (mass, energy, and position and angle of impact). Detailed simulations have demonstrated that the size of the crater produced by viscous flow scales as the inverse of the product of the cohesive energy and the melting temperature.[8] Bringa *et al.*[9] demonstrated that the lifetime of the thermal spike plays a critical role in the volume of the surface crater created by bombardment.

The lifetime of the thermal spike produced by high-energy particle bombardment depends on the rate at which the excess energy is dissipated. Conventional MD does not give an accurate representation of the energy dissipation in metals because it does not include the role of electrons in energy transport. Energetic atoms, moving in solids, lose a significant proportion of their energy to inelastic collisions with electrons. This energy loss has been included in sputtering simulations as a friction term[5,10] to represent the Lindhard model of electronic stopping. The accuracy of the friction term in describing the inelastic energy loss has been validated using time-dependent density-functional theory[11] as well as tight-binding[12,13] simulations. The energy loss to the electrons results in an excited electronic distribution, which thermalizes rapidly due to electron-electron collisions. The electronic temperature evolution, following a sputtering event, has been modeled by Duvenbeck *et al.*[14,15] by a numerical solution of the heat-transport equation for the electrons.

Previous simulations of sputtering have not included the effects of the excited electrons on the dynamics of the atoms. There is, in fact, a two-way exchange of energy between the electrons and the atoms, as hot electrons feed energy back to the lattice via electron-phonon coupling. This energy exchange was formalized in the two-temperature model (2TM).[16] Lattice and electronic temperature evolutions may then be described by a set of coupled thermal transport equations. Extensions to the 2TM have been developed in which the atomic lattice is treated explicitly using MD.[17–23] Such approaches can be generally termed 2TM-MD techniques. The electrons are incorporated into the simulations as a thermal medium that exchanges energy with the atomic degrees of freedom. This medium can store and conduct energy through the system and redistribute energy to the lattice. The strength of the coupling between the electronic medium and the atomic degrees of freedom, and thus the rate of energy exchange between the lattice and electronic subsystems, is dictated by the electron-phonon coupling parameter. The method has been used to model damage cascades in Fe (Ref. 22) and damage tracks created by swift heavy ion irradiation.[23]

In this paper we extend the methodology for including the absorption, storage, transport, and redistribution of energy by the electronic subsystem, developed for cascades, to sputtering simulations. We present results of 5 keV self-sputtering simulations in tungsten. It has been noted that the thermal spike lifetime, and thus the rate of energy dissipation, is an important parameter in determining the extent of the surface damage. An accurate representation of the electronic energy transport and redistribution is, therefore, essential for a realistic model of the surface damage resulting from bombardment. We compare the results obtained from four different models for the electronic energy transport, ranging from a model in which the role of the electrons is neglected to one in which the electronic thermal parameters have a strong dependence on the electronic and lattice temperatures. The model which neglects the electronic effects simulates the bombardment using conventional constant energy (NVE) MD simulations of an isolated system. The models which include electronic effects employ a 2TM-MD methodology. In the most complete treatment, the thermal properties of the electrons are incorporated using an electron-temperature-dependent electronic specific-heat capacity, and a lattice- and electron-temperature-dependent electronic thermal conductivity. A simpler model employs a constant electron thermal conductivity. Finally, the simplest model represents the electrons as a perfect heat bath at a constant temperature, by using a constant temperature (NVT) MD simulation method.

II. METHOD

A. Representation of the W surface

To model a W surface, we used the Finnis-Sinclair interatomic potential developed by Derlet *et al.*[24] For high-energy collisions, the short-range behavior of this potential has been modified by Björkas *et al.*[25] Simulations were performed on a cubic cell consisting of 265 302 atoms using a modified version of the DL_POLY code.[21,26] Periodic boundary conditions were imposed in two directions but not in the third producing two surfaces oriented in the (001) direction. The system was initially relaxed at constant pressure and temperature of 1 atm and 300 K, respectively. The relaxed cell dimensions were $161.4 \times 161.4 \times 164.8$ Å. The average lattice parameter in the z direction is 2% higher than the bulk, as a result of the finite size of the cell and the free boundary conditions in that dimension. The simulation cell is sufficiently large that we may assume the free boundary at the bottom does not affect the damage observed on the bombarded surface at the impact energy used. The dimensions are also sufficient to ensure that the periodic boundary conditions do not interfere with the damage created by the bombardment.

B. Modes of bombardment

For a given surface, the self-sputtering behavior depends sensitively on the impact energy, angle, and the impact position of the projectile on the surface. Particular angles and impact points promote channelling of the projectile, allowing it to penetrate deep into the solid. The resulting damage is

spread over a relatively large volume within the solid. If, on the other hand, the projectile particle has a direct collision with an atom at or near the surface, a large proportion of the impact energy may remain near to the surface, resulting in more surface damage or sputtering erosion.

This study is not meant as a complete survey of the various modes of sputtering in tungsten but is meant to elucidate the role of energy transport through conduction electrons in the resulting damage. Three different impact scenarios at 5 keV were studied. In each case, the projectile was initially located about 5 Å above the surface. In scenarios 1 and 2 the projectile is fired toward the surface at an angle of 20° to the normal. In scenario 3 the projectile velocity is perpendicular to the surface. The position of the projectile at impact with the surface for each case is different. The impact points were close to $(a/4, a/4)$ for scenarios 1 and 3, and $(0, a/2)$ for scenario 2, where the origin coincides with a surface atom and a is the lattice parameter. The perpendicular bombardment and particular impact point of scenario 3 lead to significant channelling of the projectile through nearly the full depth of the simulation cell. In scenarios 1 and 2 the impact energy remains more localized near the surface, but the behavior of the two scenarios is different due to the different impact points. These three scenarios represent different modes of bombardment in which energy is localized near the surface (1 and 2) or spreads over a significant volume within the solid (scenario 3).

C. Inclusion of thermal electronic effects

1. 2TM-MD method

The methodology used for the inclusion of thermal electronic effects in classical MD simulations is detailed in Refs. [21–23]. The method involves partitioning the atomistic simulation cell into coarse grained cells within which an electronic temperature T_e and a lattice temperature T_l are defined. These cells constitute a grid of $9 \times 9 \times 9$ cells each of which have approximately cubic dimensions of 19 Å, and each containing approximately 360 atoms. At a given time t, the lattice temperature T_l within a cell labeled n is obtained from the kinetic energy of the atoms within that cell.

$$T_{l,n}(t) = \frac{m}{3N_n k_B} \sum_{i=1}^{N_n} v_i^2, \quad (1)$$

where the sum over i runs over all N_n atoms in cell n, v_i is the velocity of atom i, k_B is Boltzmann's constant, and m is the atomic mass.

At each MD time step, energy is exchanged between the electronic heat bath and the lattice subsystem, which is represented by the atoms of the MD simulation. The energy exchange is implemented using a Langevin dynamics formalism, whereby a friction force removes energy from the atomic system, and a random force inserts energy. The friction constant γ determines the time scale on which energy is exchanged between the two subsystems $\tau = 1/\gamma$. This is related to the electron-phonon coupling parameter $g = \gamma c_l$, where c_l is the specific heat of the lattice $c_l = 3k_B\rho$ (ρ is the number density of atoms).

The loss of energy from the atomic subsystem in a time interval dt due to atoms within cell n is

$$dU_{\text{loss,n}} = \sum_{i=1}^{N_n} m\gamma v_i^2 dt. \tag{2}$$

This is related to the lattice temperature in cell n given in Eq. (1)

$$dU_{\text{loss,n}} = 3N_n k_B T_{l,n} \gamma dt. \tag{3}$$

The total gain in energy due to collisions with electrons depends on the local electronic temperature $T_{e,n}$ in cell n, and is approximately given by

$$dU_{\text{gain,n}} = 3N_n k_B T_{e,n} \gamma dt. \tag{4}$$

There is an additional stochastic term which has been neglected in Eq. (4). This term becomes small when the number of atoms is large, and there are sufficient atoms in each temperature cell, that this correction may be neglected. The net energy change per unit volume for atoms in cell n depends on the local temperature difference

$$du_n = g(T_{e,n} - T_{l,n})dt. \tag{5}$$

Energy conservation between the two subsystems is achieved by assuring that in each cell energy gained/lost by the lattice subsystem is lost/gained by the electronic subsystem. This requires the energy exchange in Eq. (5) to be accounted for in the dynamics of the electron temperature T_e. In between subsequent MD time steps, a thermal diffusion equation is evolved to update the local electronic temperature T_e in each cell. The equation for the electronic temperature is

$$c_e \frac{\partial T_e}{\partial t} = \nabla \kappa_e \nabla T_e + g(T_l - T_e), \tag{6}$$

where c_e is the electronic specific heat, κ_e is the electron thermal conductivity, and T_e and T_l depend on position and time. The first term on the RHS describes heat diffusion through the electrons, and depends on variations in the electron temperature T_e between cells. The last term, involving the electron-phonon coupling parameter g, accounts for local energy exchange between the lattice and the electrons.

The thermophysical parameters generally depend on temperature, making Eq. (6) a nonlinear partial differential equation. We use the electronic specific heat $c_e(T_e)$ for W calculated by Lin *et al.*[27] The electron thermal conductivity κ_e generally depends on T_e and T_l. A formula for $\kappa_e(T_e, T_l)$ is given in the appendix. Calculations were performed with this form of κ_e as well as a constant value κ_{e0} for comparison.

The molecular dynamics simulations performed here were evolved using a short time step of $dt_{MD}=0.1$ fs. The thermal diffusion equation for T_e was integrated numerically in between each MD time step using a fully explicit integration scheme. It was found that a time step of $dt_{TD}=dt_{MD}/2$ had to be used to evolve the thermal-conduction equation accurately. This means that the thermal diffusion equation was evolved by two time steps for each time step of the MD simulation, with the lattice temperature T_l remaining unchanged during these steps.

The method described here amounts to coupling the atoms to a heat bath representing the electrons. This heat bath has a finite heat capacity and the temperature, which is defined within electron temperature cells, varies in space and time. At the start of each simulation, the electrons are assumed to be at equilibrium with the lattice, so the electronic temperature T_e is initialized to 300 K everywhere.

2. Boundary conditions

Ideally the simulated system would have only one surface and have bulklike dimensions in the remaining directions. Due to computational restrictions, the MD cell is microscopically small, having approximate cubic dimensions of $l \sim 160$ Å. It possesses a second surface as well as periodic boundaries in the x and y directions.

The typical simulation time will be about 10 ps, which is sufficient time for the system to re-equilibrate following a bombardment event. Within the metal, heat diffuses over large distances quickly through the conduction electrons so heat loss beyond the simulation cell will have to be considered. The lattice component of thermal conductivity is very low so heat loss out of the finite simulation cell through lattice thermal conduction is negligible for the relevant time scales, and we can focus on heat loss through the electronic subsystem. The processes that would allow heat loss through the electrons from the top boundary are also too slow to be relevant for the time scales considered, so the boundary condition imposed on T_e at the top surface (located at $z=0$) is insulating

$$\left. \frac{\partial T_e}{\partial z} \right|_{z=0} = 0. \tag{7}$$

Heat transferred to the electrons in the vicinity of the bombarded region at the surface is transported to the boundary of the atomistic simulation cell within a few tens of femtoseconds. Using a value for the electronic diffusivity α_e of 116 Å^2 fs^{-1} (correct for W at 1000 K), the time taken for heat to diffuse to the edge of the atomistic simulation cell is approximately $l^2/4\alpha_e \simeq 56$ fs.

In order to transport heat away from the atomistic cell realistically, we extend the electronic subsystem beyond the atomic simulation cell in five directions, i.e., with exception of the direction from which the genuine surface is bombarded (see Fig. 1). This represents heat transport through the surrounding material. In the extended regions, the lattice temperature T_l is assumed to equal the electron temperature T_e, so there is no further energy exchange between the two subsystems.

Ideally the electronic subsystem would be extended sufficiently so that boundary conditions are irrelevant for the duration of the simulation. Alternatively, a Green's function approach for the open boundaries[15] could be used to represent heat flow beyond a certain distance. However, in order to keep the numerical integration of the diffusion equation computationally inexpensive, the electronic subsystem is only extended by about 370 Å beyond the edge of the simulation cell. The extended electronic temperature cell has approximately cubic dimensions of $L \sim 900$ Å, and comprises
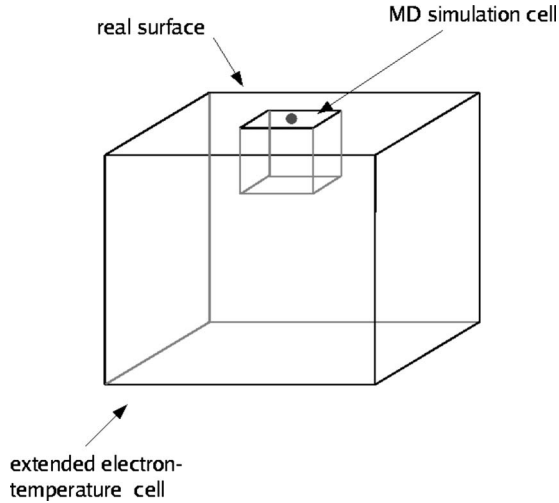
FIG. 1. Schematic showing the MD simulation cell embedded in an extended electron temperature cell. The top surface is the desired "real" surface. A circle indicates the region exposed to bombardment. The MD cell is roughly cubic with a length of 161 Å. The extended electron temperature cell has dimensions of approximately 900 Å.

$50 \times 50 \times 50$ subcells, of which only $9 \times 9 \times 9$ overlap with the MD simulation cell in which T_l is defined. Assuming a diffusivity of $\alpha \sim 116$ m^2 K^{-1}, the time taken for heat to traverse the extended cell from the middle of the exposed surface is about $L^2/4\alpha_e \sim 1.2$ ps.

In order to assess whether this extension is sufficiently large, so that the boundary conditions on the extended electron temperature cell are of no consequence to the results, we compared two simulations in which different boundary conditions were used at the extended boundaries. In the first simulation, the electronic temperature at the five extended boundaries was fixed to $T_{e0} = 300$ K, allowing heat to leave the system at the extended boundaries

$$T_e(\pm L/2, y, z, t) = T_e(x, \pm L/2, z, t) = T_e(x, y, -L, t) = T_{e0}. \tag{8}$$

In the second simulation, insulating boundary conditions were used at the five extended boundaries

$$\left. \frac{\partial T_e}{\partial x} \right|_{x=\pm L/2} = \left. \frac{\partial T_e}{\partial y} \right|_{y=\pm L/2} = \left. \frac{\partial T_e}{\partial z} \right|_{z=-L} = 0. \tag{9}$$

In both cases the insulating boundary condition (7) was applied to the real surface at $z=0$. The maximum electronic temperature within the system was monitored and it was found that the electron temperatures in the two simulations start to differ after about 1 ps. As expected, the fully insulated system maintains a higher maximum temperature than the system with fixed temperature boundary conditions, from which heat can escape out of the five extended boundaries. The difference between the two maximum electron temperatures is small, however, and only reaches approximately 25 K after 10 ps. For this reason, the dimensions of the extended electron subsystem are regarded as being sufficiently large for the effect of the extended boundaries on T_e to be small.

The fixed boundary conditions [Eq. (8)] together with Eq. (7) were applied in all simulations for which the 2TM-MD method was used.

D. Comparison between simulation methods

The aim of this work is to assess the influence of electronic effects on the damage caused by surface bombardment. Each of the three bombardment scenarios is simulated using four different methods.

In the first method, which we denote by NVE, electronic effects are neglected altogether. The system is simulated within the microcanonical ensemble, which means energy does not enter or leave the atomic subsystem. All of the bombardment energy remains inside the atomistic simulation cell.

In the next two methods, electronic effects are included using the 2TM-MD method described above to describe energy exchange between the lattice and electron subsystems. Two distinct 2TM-MD approaches are compared in order to assess sensitivity of the results to the electronic thermal parameters. In the first, which we denote by 2TM-MD-const, a constant electronic thermal conductivity $\kappa_{e,0} = 146$ W m^{-1} K^{-1} is used to describe thermal conduction through the electrons. This value corresponds to the experimental thermal conductivity of W at 500 K. A more refined representation of the thermal properties of the electrons is used in 2TM-MD-var, where a variable $\kappa_e(T_e, T_l)$ is used, as given in the appendix. It should be noted that in both 2TM-MD approaches, the electronic specific heat $c_e(T_e)$ is temperature dependent, so that the electronic diffusivity is temperature dependent in both models.

In the fourth approach, denoted by NVT, the electronic system is represented in a simplified manner as an ideal heat bath, by employing a Langevin thermostat with a bath temperature of 300 K everywhere in the simulation cell. This perfect heat bath may be viewed as taking the electronic subsystem to have an infinite heat capacity or an infinite thermal conductivity, preventing an elevation of the electron temperature.

All cases in which energy is exchanged with the electronic subsystem (2TM-MD-const, 2TM-MD-var, and NVT), employ the same electron-phonon coupling constant $g = 7.0 \times 10^{17}$ W m^{-3} K^{-1} which falls within the range $1-10 \times 10^{17}$ W m^{-3} K^{-1} deduced from pulsed laser experiments by Fujimoto *et al.*[28] This coupling constant corresponds to an inverse time scale of $\gamma = 0.27$ ps^{-1} for the Langevin equation. In terms of the electron heat bath, the location of the top surface was assumed to be fixed at $z=0$. This means that coupling to the heat bath (in 2TM-MD-const, 2TM-MD-var, and NVT) via friction and stochastic forces only occurs for atoms below this rigidly defined surface. Atoms above $z=0$ move freely under Newton's equations of motion.

III. RESULTS

A. Extent and distribution of damage caused by bombardment

The results obtained here are from 12 separate simulations consisting of bombardment scenarios 1, 2, and 3 simulated
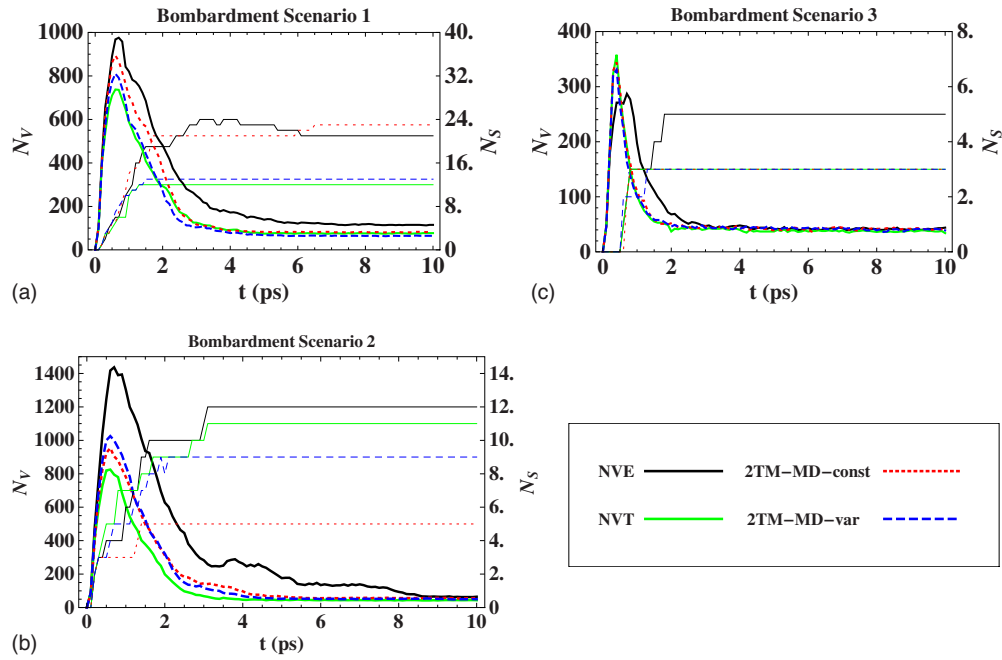
FIG. 2. (Color online) Thick lines: number of vacancies N_V. Thin lines: number of sputtered particles N_s produced as a function of time t during bombardment simulations.

using four methods: NVE, NVT, and 2TM-MD methods with constant and variable κ_e.

The damage caused in the material as a result of bombardment is defined in terms of the defects formed. These are identified by comparing the atomic configuration to the initially equilibrated lattice configuration. Sites from which atoms have been displaced by more than 1 Å are considered vacancies. The displaced atoms constitute: sputtered atoms if

they reach a height of 10 Å or more above the surface, interstitials if they are deeper than the first atomic layer of the surface, and adatoms which sit on top of the surface.

The thick lines in Fig. 2 show the evolution of the total number of vacancies against time for each simulation. Upon impact by the projectile a large number of defects are formed initially, most of which are subsequently repaired as the system relaxes. The remaining damage is the residual damage. It

TABLE I. Summary of damage caused by bombardments. Total number of vacancies N_V, vacancies in the surface layer N_{V_s} (as a proportion of all vacancies in brackets), N_S sputtering yield, N_A adatoms, and N_I interstitials (N_S, N_A, N_I as a proportion of the total number of displaced atoms in brackets).

| Simulation	N_V	N_{V_s}	N_S	N_A	N_I
Scenario 1					
NVE	114	37 (0.32)	21 (0.18)	90 (0.78)	4 (0.04)
NVT	76	26 (0.34)	12 (0.16)	55 (0.71)	10 (0.13)
2TM-MD-const	81	29 (0.36)	23 (0.28)	52 (0.63)	7 (0.09)
2TM-MD-var	64	29 (0.45)	13 (0.2)	40 (0.62)	12 (0.19)
Scenario 2					
NVE	64	18 (0.28)	12 (0.19)	51 (0.79)	2 (0.03)
NVT	44	19 (0.43)	11 (0.24)	24 (0.53)	10 (0.22)
2TM-MD-const	55	16 (0.29)	5 (0.09)	46 (0.82)	5 (0.09)
2TM-MD-var	49	15 (0.31)	9 (0.18)	36 (0.72)	5 (0.10)
Scenario 3					
NVE	43	7 (0.16)	5 (0.11)	9 (0.21)	30 (0.68)
NVT	33	9 (0.27)	3 (0.09)	11 (0.32)	20 (0.59)
2TM-MD-const	42	11 (0.26)	3 (0.07)	12 (0.28)	28 (0.65)
2TM-MD-var	38	9 (0.24)	3 (0.08)	12 (0.31)	24 (0.62)
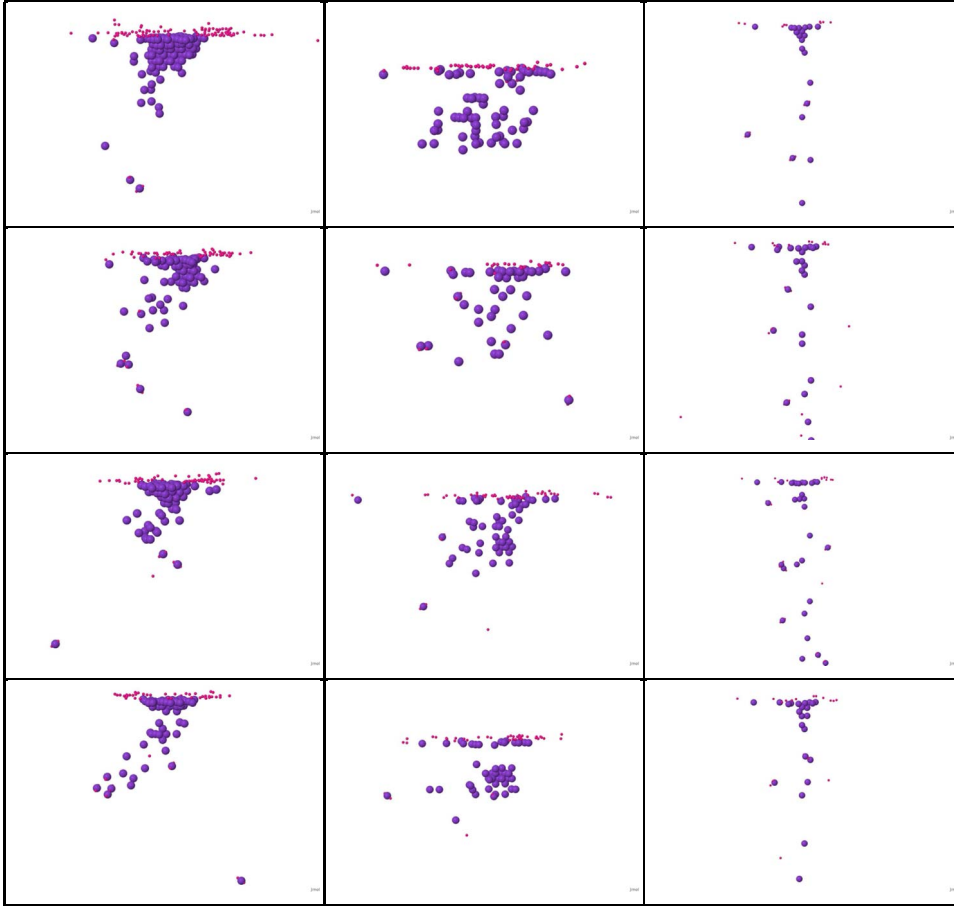
FIG. 3. (Color online) Images of final defect configurations, 10 ps after bombardment. Large spheres represent vacancies and small spheres are displaced atoms. Sputtered atoms are not shown. The three columns are for bombardment scenarios 1, 2, and 3, respectively. The four rows are for simulation methods NVE, NVT, 2TM-MD-const, and 2TM-MD-var, respectively. The bombarded surface is the horizontal plane above which there are no more vacancies. Adatoms on the surface are visible.

can be seen that results for the various impact scenarios differ significantly as well as the results using different simulation methods for the same scenario. In bombardment scenarios 1 and 2, the total number of defects formed initially is clearly highest for the NVE method in which all of the energy remains in the simulation cell, however, this extra energy also allows for significant repair of the damage through annealing, so that the residual damage relative to the maximal damage is relatively small. In scenario 3, in which the projectile channels deep into the material, less defects are initially formed with the NVE method. This is because, out of the four methods, this is the only one that does not involve a friction force acting on the atoms in the solid. This allows the projectile to channel further into the solid before transmitting energy to other atoms through collisions.

The thinner lines in Fig. 2 show the sputtering yield N_s, defined as the number of particles reaching a height of 10 Å above the surface, as a function of time. Scenario 1 results in the most sputtering followed by scenario 2 and then scenario 3. Within each scenario, the NVE method generally gives rise to the most sputtering.

Table I summarizes the residual damage remaining at the end of each simulation. The damage is quantified in terms of the total number of vacancies N_V, vacancies in the first atomic layer N_{Vs}, sputtered atoms N_S, adatoms N_A, and interstitial atoms N_I found at the end of each simulation.

The various simulation methods differ in the way in which heat is stored and transported throughout the system. It is interesting to find out not only how this affects the total

amount of damage in terms of the number of defects but also the nature of this damage as characterized by the spatial distribution of defects. In particular we are interested in surface damage. This consists of isolated vacancies at the surface, larger craters, and adatoms. The most severe kind of surface damage consists of craters. These are defined as clusters of vacancies that are connected to the surface. A vacancy cluster is defined as a group of vacancies that are within one lattice parameter of each other.

Figure 3 shows defects identified at the end of each simulation. The bombarded surface is the horizontal plane that is demarcated by the last row of vacancies. A visual inspection reveals that the surface damage is different in each case. Bombardment scenario 1 produces deep craters whereas bombardment scenario 2 forms smaller, shallower craters. Bombardment scenario 3 results in little surface damage but defects are created along a track that extends almost to the bottom of the slab in a direction perpendicular to the surface.

The characteristics of damage, produced in the various simulations that can be seen in Fig. 3, are quantified using several different metrics in Table II. The first column lists all vacancy clusters found in terms of their size. In most cases, the largest cluster is connected to the surface and constitutes the main crater. This is quantified by N_{MC}, the size of the main crater in atomic volumes. N_{MCs} is the number of vacancies in the main crater that are located in the plane of the first atomic layer. This is a measure of the size of the opening of the crater at the surface. Such metrics give information not only about the size of the largest crater, but also the depth of

TABLE II. Description of the distribution of vacancies. The first column lists clusters in terms of their size (multiple clusters of the same size are indicated using "number×size" notation). N_{MC} number of vacancies constituting the main crater (defined in text). N_{MCs} is the number of vacancies in the crater that are in the first atomic layer (i.e., size of the opening of crater). V_V is the volume per vacancy obtained from the ellipsoidal analysis method (explained in the text).

Simulation	Clust.	N_{MC}	N_{MC}/N_V	N_{MCs}	N_{MCs}/N_{MC}	V_V (Å³)
Scenario 1						
NVE	(93,3,2)	93	0.82	31	0.33	7.9
NVT	(44,4,2×2)	44	0.58	15	0.34	22.8
2TM-MD-const	(53,4,3,3×2)	53	0.65	21	0.4	11.4
2TM-MD-var	(34,7,2)	34	0.53	23	0.68	27.1
Scenario 2						
NVE	(13,8,5,4, 2×3,6×2)	13	0.2	8	0.62	23.0
NVT	(15,3,2)	15	0.34	11	0.73	52.7
2TM-MD-const	(16,11,3×2)	11	0.2	4	0.36	36.6
2TM-MD-var	(21,3,6×2)	2[a]	0.04	2	1.0	27.7
Scenario 3						
NVE	(9,4,3,2×2)	9	0.21	4	0.44	168.5
NVT	(10,2)	10	0.3	5	0.5	191.0
2TM-MD-const	(4,3,4×2)	3[b]	0.07	3	1.0	213.0
2TM-MD-var	(10,3,4×2)	10	0.26	5	0.5	94.4

[a]No craters, but three vacancy dimers on the surface.
[b]No craters, but one trimer of vacancies at the surface.

the damage. It is clear that scenario 1 produces the largest craters, with the largest being produced by the NVE simulation method. This is consistent with the viscous flow mechanism.[5] The 2TM-MD-var method gives rise to the smallest crater, which is also proportionately the shallowest one (i.e., with the largest proportion of the constituting vacancies at the surface). Scenario 2 produces small craters with a high percentage of the vacancies on the surface layer. The tracklike defect distribution of scenario 3 resembles that of a linear cascade.

Finally we use the ellipsoidal analysis of Hou[29] to characterize the overall spread of vacancies. This method produces an ellipsoid whose dimensions are determined by the standard deviation of vacancies from the mean vacancy position along three principal directions. V_V is the volume (in cubic Angstroms) of the ellipsoid characterizing the residual vacancies, divided by the total number of residual vacancies. V_V is a measure of the spread of the vacancies. In scenarios 1 and 2, V_V is clearly smaller for the NVE simulations than the rest. One explanation for this may be that the additional heat available to the system (as no heat leaves the system) allows for more annealing of defects, leading to more vacancy clustering. The NVT simulations lead to more diffuse vacancy distributions as the system cools rapidly and defects are quenched in position. The two 2TM-MD methods show different behaviors of V_V in each case. The ellipsoid volumes for scenario 3 are generally large as the projectile penetrates deep into the simulation cell producing a trail of defects

along its track. Since atoms in the 2TM-MD-const, 2TM-MD-var, and NVT methods experience friction (energy loss to the electron subsystem), the range of the projectile is somewhat lower in these cases, making the comparison to the NVE simulations unfair. Nevertheless it can be seen that the NVE method gives rise to compact distributions of vacancies compared to the other three methods. The 2TM-MD-var method, involving the temperature-dependent electronic thermal conductivity model, appears to give compact distributions in scenarios 2 and 3 and a diffuse distribution in scenario 1.

B. Electron and lattice temperatures

The four simulation methods differ in terms of how heat is dissipated through the system, and this affects the extent to which the initial damage is quenched. Figure 4 shows the lattice temperature near the top of the MD simulation cell against time, for bombardment scenario 2, simulated using all four methods. This temperature is calculated using the average kinetic energy for atoms located in the top layer of temperature cells. It is seen that the temperatures are highest for the NVE simulations, in which heat remains in the atomic system while the system cools down using the other three methods. Lattice temperature profiles, along the z direction, at $t=2$ ps are shown in Fig. 5. Temperatures are generally highest for NVE simulations, and lowest for NVT simulations (in which a homogeneous thermostat at $T=300$ K is
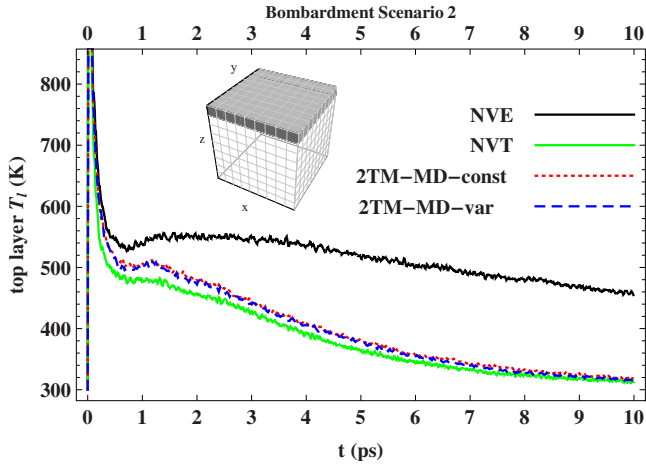
FIG. 4. (Color online) Average lattice temperature in the top layer of temperature cells against time for scenario 2 using all four methods. The inset shows the cells from which this lattice temperature is obtained.

used). In Fig. 5 it can be seen that after 2 ps most of the heat in bombardment scenarios 1 and 2 is located near the surface of the simulation cell. The average surface temperature is higher for scenario 2 than for scenario 1 and this may be responsible for the shallow craters created in this scenario. For bombardment scenario 3 the energy of the projectile is deposited deeper inside the metal. The effect of the friction force for simulations using the 2TM-MD-const, 2TM-MD-var, and NVT methods is evident in the figure for bombardment scenario 3, as the majority of heat deposition occurs

closer to the surface for these than in the NVE simulation.

Atoms simulated using the NVT method are subjected to a conventional thermostat at 300 K at all times. The 2TM-MD-const and 2TM-MD-var methods involve thermostatting atoms according to the local electronic temperature T_e, which depends on position and time. Differences between method 2TM-MD-const, in which a constant electron thermal conductivity $\kappa_{e0} = 146$ W m^{-1} K^{-1} (appropriate for 500 K) is used to evolve T_e, and method 2TM-MD-var, in which the variable $\kappa_e(T_e, T_l)$ given in the appendix is used, are more easily seen in the electronic temperature T_e. Figure 6 contrasts the maximum electron temperature in the simulation cell against time for both methods for the case of scenario 2. At early times, the maximum T_e is higher for method 2TM-MD-var than 2TM-MD-const. At later times, when the system cools down, temperatures are higher for method 2TM-MD-const as $\kappa_e(T_e, T_l) > \kappa_{e,0}$ at low temperatures. Profiles of the electronic temperature near the bombarded surface at $t = 0.2$ ps are shown in Fig. 7. At these early times, a short time after the projectile impacts the surface, the profiles for method 2TM-MD-var are generally more peaked. Method 2TM-MD-var gives rise to higher temperatures in the hot regions, and lower temperatures in the cooler regions, compared with 2TM-MD-const.

It should be noted that the effect of electron-phonon coupling on atomic motion manifests itself after a relatively long time. The time scale is dictated by $\tau = 1/\gamma = c_l/g$, which takes a value of 3.7 ps in these simulations. However, plots in Figs. 2 and 4 indicate that differences in the number of defects formed and the lattice temperature start to emerge after 0.5 ps or even earlier.
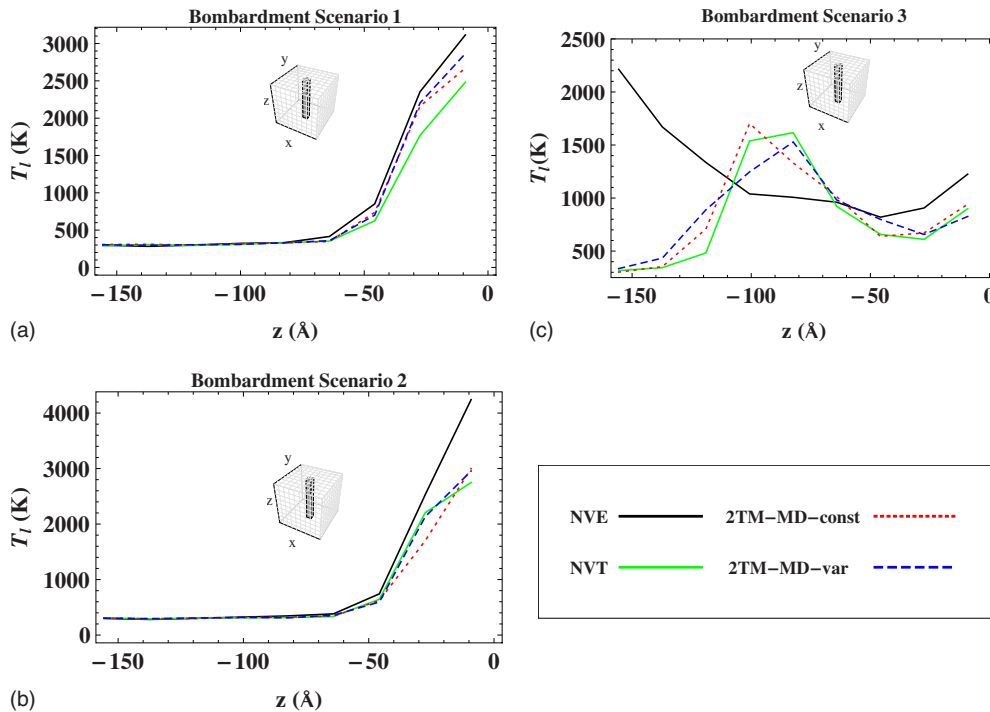

FIG. 5. (Color online) Lattice temperature profiles at $t = 2$ ps. The profiles, $T_l(0, 0, z, t = 2$ ps), correspond to the lattice temperatures within the central column of temperature cells indicated in the inset. The surface is located at $z = 0$. In scenario 3, the maximum temperature occurs near the bottom end of the simulation cell for the NVE method, and at a shallower depth for the other three methods, as the friction experienced by the projectile in these methods decreases the range it travels through the metal before depositing most of its energy.
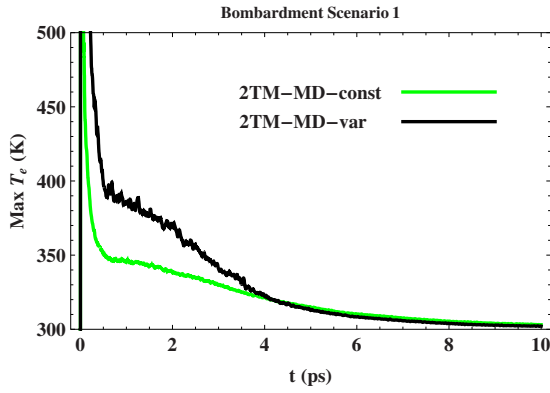
FIG. 6. (Color online) Maximum electron temperature T_e in the simulation cell against time, for simulations of bombardment scenario 1, employing the two distinct 2TM-MD methods. Method 2TM-MD-const is based on fixed electron thermal conductivity $\kappa_{e,0} = 146$ W m^{-1} K^{-1}. Method 2TM-MD-var uses the temperature-dependent version $\kappa_e(T_e, T_l)$ given in the appendix.

IV. CONCLUSION

We have developed a hybrid electronic thermal diffusion MD method for sputtering simulations that includes the effect of energy loss due to electronic stopping and redistribution by electron-phonon coupling. The method was used to model 5 keV self-sputtering of tungsten. The broad structural features of the damaged surface structure were found to be very sensitive to the direction and point of impact of the bombarding atom. The detailed features of the damaged surface were found to be sensitive to model used to dissipate the excess energy of fast-moving atoms. Constant energy simulations (NVE) generally created the most damage due to the higher temperatures reached. This showed up as larger craters for bombardment scenarios in which the energy is localized close to the surface. The bombardment that resulted in channelling deep into the sample showed less variation in damage between the four thermal models explored.

Simulations in which energy was dissipated by coupling to the electronic system, to represent the electronic thermal conductivity of the metal, appeared to show some sensitivity to the model used for the electronic thermal properties. The variations were small, however, and may not be statistically significant. Nevertheless, the simulations in which the electronic energy was stored and fed back into the lattice (2TM-MD-const and 2TM-MD-var) displayed an enhanced tendency for vacancy clustering in the subsurface region, which is consistent with the slower lattice cooling, thus enhanced annealing, associated with this method as compared to the NVT method in which energy is dissipated into a perfect heat bath.

These results show that the characteristics of damage caused by sputtering such as vacancy distributions and crater morphology depend on how heat is transported around the system, and are sensitive to the model used for electronic thermal transport. These findings have implications for comparisons between experimentally observed sputtering damage and molecular dynamics simulation results. Vacancy radial distribution functions and measures, quantifying vacan-
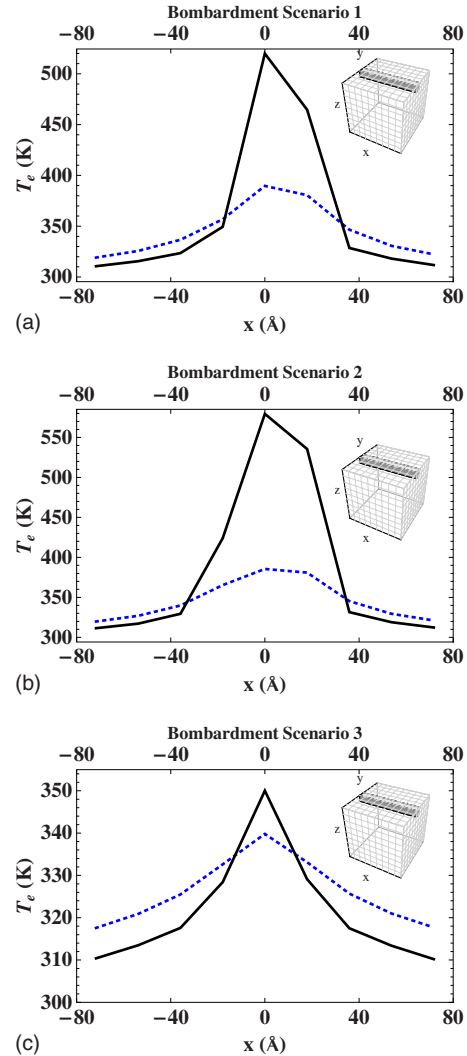

FIG. 7. (Color online) Electron temperature profiles at t = 0.2 ps using methods 2TM-MD-const (dotted line) and 2TM-MD-var (full line). The profiles, $T_e(x,0,0,t=0.2$ ps), are taken from a row of cells near the top of the simulation cell, as shown in the inset. Only electron temperature cells overlapping the MD simulation cell are shown here. Method 2TM-MD-const is based on fixed electron thermal conductivity $\kappa_{e,0} = 146$ W m^{-1} K^{-1}. Method 2TM-MD-var uses the temperature-dependent version $\kappa_e(T_e, T_l)$ given in the appendix.

cy clustering used in Ref. 10 to compare MD simulations to field-ion microscopy studies, are likely to be influenced by the use of a 2TM-MD method to incorporate electronic heat transport into the MD simulations. From our results it is clear that simulations in which electronic thermal transport is included within some approximation give substantially different results to simulations in which it is neglected altogether. Further simulations are required to make more quantitative comparisons between the vacancy distributions produced with the various methods, and allow comparisons to experimental observations.

The simulations were carried out for tungsten because of the interest in this metal as a plasma-facing material. Tungsten has a high electronic thermal conductivity, and consequently a low electron-phonon coupling constant, therefore,

electronic effects are expected to be relatively small. Other metals (e.g., Ti, Nb, V, and Fe) have lower thermal conductivity and higher electron-phonon coupling,[30] both of which would strongly enhance the effects discussed in this paper.

APPENDIX: ELECTRONIC THERMAL CONDUCTIVITY OF W

A commonly used expression for the electronic thermal conductivity of a metal under nonequilibrium conditions (when $T_e \neq T_l$) is[15,17,18]

$$\kappa_e(T_e, T_l) = \frac{1}{3} c_e(T_e) v_F^2 \frac{1}{aT_e^2 + bT_l}, \qquad \text{(A1)}$$

where c_e is the electronic specific heat, v_F is the Fermi velocity of the electrons, and T_e and T_l are the electron and lattice temperatures, respectively. The denominator expresses the frequency of collisions $1/\tau_e$ suffered by conduction electrons as a result of electron-electron and electron-phonon collision frequencies $1/\tau_{ee}$ and $1/\tau_{ep}$, which depend on T_e^2 and T_l, respectively

$$\frac{1}{\tau_e} = \frac{1}{\tau_{ee}} + \frac{1}{\tau_{ep}}. \qquad \text{(A2)}$$

Values for the coefficients a and b exist in the literature, for example, for gold $a = 1.2 \times 10^7$ K^{-2} s^{-1} and $b = 1.23 \times 10^{11}$ K^{-1} s^{-1}.[18] For nickel $a = 1.4 \times 10^6$ K^{-2} s^{-1} and $b = 1.624 \times 10^{13}$ K^{-1} s^{-1}.[18] For copper $a = 1.75 \times 10^7$ K^{-2} s^{-1} and $b = 1.98 \times 10^{11}$ K^{-1} s^{-1}.[17]

Since values of a and b for W are not available, we obtain them here by fitting to experimental values of the thermal conductivity of tungsten κ_{exp}. The data, taken from Ref. 31, consist of the thermal conductivity at different temperatures T. Only the higher temperature range from 300 up to 2000 K of the data was used for fitting. The experiments are assumed to take place under equilibrium conditions $T_e = T_l = T$. In principle κ_{exp} consists of the lattice and electron contributions to thermal conductivity κ_l and κ_e. Since κ_l is generally on the
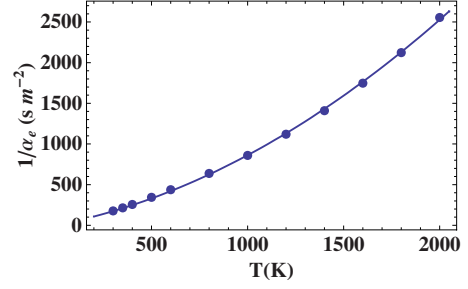

FIG. 8. (Color online) Plot of $1/\alpha_e$ against T. The points are experimental data for $1/\kappa_{\text{exp}}$ from Ref. 31 multiplied by c_e from Ref. 27 at the appropriate temperature. The line is a fit to $AT^2 + BT$.

order of 1–10 W m^{-1} K^{-1} in metals,[32] it makes up only a few percent of the measured thermal conductivity κ_{exp}, so we can assume $\kappa_{\text{exp}} \simeq \kappa_e$.

To proceed with fitting, we first divide the experimental values for $\kappa_{\text{exp}}(T)$ by the corresponding values of $c_e(T)$ from Ref. 27, to obtain the electronic diffusivity $\alpha_e = \kappa_e / c_e$. According to Eq. (A1), the reciprocal of this should be

$$\frac{1}{\alpha_e} = AT^2 + BT, \qquad \text{(A3)}$$

where $A = 3a/v_F^2$ and $B = 3b/v_F^2$. Fitting the data points to Eq. (A3), we obtained values of $A = 4.02 \times 10^{-4}$ s m^{-2} K^{-2} and $B = 0.460$ s m^{-2} K^{-1}. Figure 8 shows a plot of the data points used together with the fitting result. To see how the values obtained compare with other metals, we take rough estimate of the Fermi velocity $v_F \simeq 10^6$ m s^{-1} to get $a \simeq 1.34 \times 10^8$ s^{-1} K^{-2} and $b \simeq 1.53 \times 10^{11}$ s^{-1} K^{-1}. At 300 K, these values correspond to collision times $\tau_{ep} \sim 20$ fs and $\tau_{ee} \sim 80$ fs.

It should be noted that κ_e is obtained from A and B directly, and this value of v_F is being used for comparative purposes only and not for the calculations requiring κ_e themselves. The expression used in the calculations is

$$\kappa_e(T_e, T_l) = \frac{c_e(T_e)}{AT_e^2 + BT_l}. \qquad \text{(A4)}$$

In summary, we have used experimental thermal conductivity data, which are obtained under near-equilibrium conditions $T_e \simeq T_l$, to obtain parameters for an expression κ_e suitable to nonequilibrium conditions.

[1] H. Bolt, V. Barabash, W. Krauss, J. Linke, R. Neu, S. Suzuki, N. Yoshida, and ASDEX Upgrade Team, J. Nucl. Mater. **329-333**, 66 (2004).

[2] V. Barabash, J. Nucl. Mater. **329-333**, 156 (2004).

[3] E. Salonen, K. Nordlund, J. Keinonen, and C. H. Wu, J. Nucl. Mater. **313-316**, 404 (2003).

[4] W. Eckstein and J. Lszl, J. Nucl. Mater. **183**, 19 (1991).

[5] M. Ghaly, K. Nordlund, and R. Averback, Philos. Mag. A **79**, 795 (1999).

[6] G. Betz and W. Husinsky, Philos. Trans. R. Soc. London, Ser. A **362**, 177 (2004).

[7] Z. Insepov, J. Norem, D. Swenson, A. Hassanein, and M. Terasawa, Nucl. Instrum. Methods Phys. Res. B **258**, 172 (2007).

[8] K. Nordlund, K. O. E. Henriksson, and J. Keinonen, Appl. Phys. Lett. **79**, 3624 (2001).

[9] E. M. Bringa, K. Nordlund, and J. Keinonen, Phys. Rev. B **64**, 235426 (2001).

[10] Y. Zhong, K. Nordlund, M. Ghaly, and R. S. Averback, Phys. Rev. B **58**, 2361 (1998).

[11] M. Lindenblatt, E. Pehlke, A. Duvenbeck, B. Rethfeld, and A. Wucher, Nucl. Instrum. Methods Phys. Res. B **246**, 333 (2006).

[12] D. Mason, J. le Page, C. Race, W. Foulkes, M. Finnis, and A. Sutton, J. Phys.: Condens. Matter **19**, 436209 (2007).

[13] J. le Page, D. Mason, C. Race, and W. Foulkes, New J. Phys. **11**, 013004 (2009).

[14] A. Duvenbeck, F. Sroubek, Z. Sroubek, and A. Wucher, Nucl. Instrum. Methods Phys. Res. B **225**, 464 (2004).

[15] A. Duvenbeck and A. Wucher, Phys. Rev. B **72**, 165408 (2005).

[16] M. I. Kaganov, I. M. Lifshitz, and L. V. Tanatarov, Sov. Phys. JETP **4**, 173 (1957).

[17] C. Schafer, H. M. Urbassek, and L. V. Zhigilei, Phys. Rev. B **66**, 115404 (2002).

[18] D. S. Ivanov and L. V. Zhigilei, Phys. Rev. B **68**, 064114 (2003).

[19] D. S. Ivanov and L. V. Zhigilei, Appl. Phys. A **79**, 977 (2004).

[20] Y. Yamashita, T. Yokomine, S. Ebara, and A. Shimizu, Fusion Eng. Des. **81**, 1695 (2006).

[21] D. Duffy and A. Rutherford, J. Phys.: Condens. Matter **19**, 016207 (2007).

[22] A. Rutherford and D. Duffy, J. Phys.: Condens. Matter **19**, 496201 (2007).

[23] D. Duffy, N. Itoh, A. Rutherford, and A. Stoneham, J. Phys.: Condens. Matter **20**, 082201 (2008).

[24] P. M. Derlet, D. Nguyen-Manh, and S. L. Dudarev, Phys. Rev. B **76**, 054107 (2007).

[25] C. Björkas, K. Nordlund, and S. Dudarev, Nucl. Instrum. Methods Phys. Res. B (to be published).

[26] W. Smith and T. R. Forester, J. Mol. Graphics **14**, 136 (1996).

[27] Z. Lin, L. V. Zhigilei, and V. Celli, Phys. Rev. B **77**, 075133 (2008).

[28] J. G. Fujimoto, J. M. Liu, E. P. Ippen, and N. Bloembergen, Phys. Rev. Lett. **53**, 1837 (1984).

[29] M. Hou, Phys. Rev. B **31**, 4178 (1985).

[30] T. Qiu and C. Tien, Int. J. Heat Mass Transfer **35**, 719 (1992).

[31] *CRC Handbook of Chemistry and Physics*, 88th ed., edited by D. R. Lide (CRC Press, London, 2007).

[32] R. Berman, *Thermal Conduction in Solids, Oxford Studies in Physics* (Clarendon Press, Oxford, 1979).